# Spin-Selective Trifunctional Metasurfaces for Deforming Versatile Nondiffractive Beams along the Optical Trajectory

*Tianyue Li, Yun Chen, Boyan Fu, Mengjiao Liu, Jinwen Wang,\* Hong Gao, Shuming Wang,\* and Shining Zhu*

Exploring and taming the diffraction phenomena and divergence of light are foundational to enhancing comprehension of nature and developing photonic technologies. Despite the numerous types of nondiffraction beam generation technologies, the 3D deformation and intricate wavefront shaping of structures during propagation have yet to be studied through the lens of nanophotonic devices. Herein, the dynamic conversion of a circular Airy beam (CAB) to a Bessel beam with a single-layer spin-selective metasurface is demonstrated. This spatial transformation arises from the interplay of 1D local and 2D global phases, facilitating the 3D control of non-diffractive light fields. An additional overall phase gradient and orbital angular momentum are introduced, which effectively altering the propagation direction and transverse fields of complex amplitude beams along the optical path. The manifested samples exhibit superior defect resistance, laying a crucial application in micro/nanolithography technologies. This approach expands the in-plane spin-selective mechanism and leverages the out-of-plane propagation dimension, allowing for integrated high-resolution imaging, on-chip optical micromanipulation, and micro/nanofabrication within a versatile nanophotonic platform.

## 1. Introduction

Diffraction is a fundamental physical phenomenon exhibited by light as it propagates through free space, manifesting as divergence after traveling a finite distance. However, the specific solutions to wave equations theoretically violate this phenomenon, allowing for the development of nondiffracting beams.[1,2] Bessel beams (BBs) serve as a prime example, propagating indefinitely along the optical axis and maintaining their intensity distributions across transverse planes.[3] Thus, BBs have gained prominence in various applications, such as light-sheet imaging,[4–7] multiparticle trapping,[8] and high-aspect-ratio waveguide fabrication.[9–11] In 2007, the Airy beam (AB), which follows a curved trajectory, was reported as a unique solution to the Schrödinger equation.[12–14] With self-focusing, self-accelerating, and self-healing attributes, this beam has become a pivotal tool in numerous applications, such as scanning imaging[15–18] and particle transport.[19–21] Furthermore, other nondiffraction beams, including the Mathieu[22,23] and cosine beams,[24] have expanded this field.

Because of the strong demand for increased precision in advanced optical platforms, which require compact devices and diffraction-limit spots, fervent interest has ignited in achieving such beams in the field of nanophotonics, especially concerning metasurfaces for generating nondiffraction fields.[25–36] Subsequently, a challenge has arisen from the unchangeable trend of microstructures resulting in a fixed nanophotonic field after postfabrication. To overcome this issue, a multifunctional, multidimensional, and controllable nondiffraction generator is needed, requiring novel versatility and flexibility in phase modulation and leveraging the

T. Li, B. Fu, M. Liu, S. Wang, S. Zhu
National Laboratory of Solid-State Microstructures
School of Physics
Nanjing University
Nanjing, Jiangsu 210093, China
E-mail: wangshuming@nju.edu.cn
T. Li, B. Fu, M. Liu, S. Wang, S. Zhu
Collaborative Innovation Center for Advanced Microstructures
Nanjing University
Nanjing, Jiangsu 210093, China

Y. Chen, J. Wang, H. Gao
Ministry of Education Key Laboratory for Nonequilibrium Synthesis and Modulation of Condensed Matter
Shaanxi Province Key Laboratory of Quantum Information and Quantum Optoelectronic Devices, School of Physics
Xi'an Jiaotong University
Xi'an, Shanxi 710049, China
E-mail: jinwenwang@xjtu.edu.cn
Y. Chen
School of Science
Huzhou University
Huzhou, Zhejiang 313000, China
S. Wang, S. Zhu
Key Laboratory of Intelligent Optical Sensing and Manipulation Ministry of Education
Nanjing University
Nanjing, Jiangsu 210093, China

**ADVANCED
SCIENCE NEWS**

www.advancedsciencenews.com

**LASER
& PHOTONICS
REVIEWS**

www.lpr-journal.org

degrees of freedom (DoFs) inherent to the physical mechanism of nanoantennas. Notably, the TAM plate is capable of achieving independent orbital angular momentum (OAM) conversion along its propagating direction and switching between two polarization channels,[37,38] raising the question of whether it is feasible to not only achieve the conversion of various nondiffraction beams during propagation but also endow them with complex structured phases. Although previous works have demonstrated the transformation of circular Airy beams (CABs) to BBs in bulk optics,[39–42] full control over the focal length and beam structure along the optical axis is still not possible, and the superposition of complex phases remains elusive.

In this work, we introduce a general method for experimentally demonstrating propagation-deformable CABs by leveraging both local and global phase modulation process. This approach intuitively reduces complexity into 1D basic modulation and 2D overall modulation, corresponding to the generation and manipulation of controllable CABs and structured phase distributions, respectively. This technique facilitates the generation of 3D nondiffraction structured beams on metasurfaces with adjustable focal lengths and directions. In addition, this procedure expands upon the beam generation process to realize on-demand tri-functional spin–switchable and versatile behaviors. By employing our modulation mechanism, we formulate a diffraction model for the transformation from CABs to BBs, incorporating both local and global phase information, and we outline metasurface design criteria based on phase delay differences. Moreover, given the inherent robustness of the resistance of nondiffraction beams to defects during propagation, we show that the proposed device can develop imperfections without affecting the quality of the light field, which is crucial for durability in nanoscale lithography. Our work propels the frontier of nondiffraction beam generation and manipulation, enhancing control and versatility in laser direct writing, enabling high-resolution microscopy with concurrent light-sheet and scanning functionalities, and optimizing strategies for multiparticle transport and trapping.

## 2. Results

We have two objectives: 1) to design a nondiffractive beam with a structured profile that varies along the propagating axis and 2) to develop a multifunctional meta-device with switchability. **Figure 1a** shows the proposed cases of autofocusing and autodefocusing circular Airy beams (AFCAs and ADCAs, respectively) that are transformed into BBs as they propagate axially. The beam transformation process is underpinned by the intertwined contributions of two different phase mechanisms: local and global phases. Figure 1b depicts this relationship, with the yellow arrows pointing to the radial direction that governs local phase characteristics, such as those found at a specific radius on the metasurface. Similarly, the red highlighted area, encompassing the entirety of the sample, can dictate the mathematical formulation of the phase profile, covering 2D coordinated parameters and beyond. In the following section, we delve into the mechanics of the CAB to BB transformation, revisiting the Airy functions documented in previous literature. This review provides a foundation for 3D structural manipulation of nondiffraction light fields. We then detail our proposed

mechanism for modulating both local and global phases and illustrate how it reshapes CAB. By building upon the properties of CAB and introducing the fundamentals of multifunctional metasurface design, we can achieve our envisioned spin-dependent multifunctionality.

### 2.1. Theoretical Formulation of CAB to BB Conversion

The Airy beam represents a particular solution for monochromatic electromagnetic waves.[43,44] In a 1D scenario along the radial direction, the intensity oscillation described by the radial coordinate is as follows:[39]

$$\psi(r) = Ai\left[\pm\left(\frac{r_0 - r}{\omega}\right)\right]\cdot\exp\left[\pm\alpha\left(\frac{r_0 - r}{\omega}\right)\right] \tag{1}$$

where $Ai$ is the Airy function, symbol $\pm$ indicates whether the intensity decays of the side lobes inward or outward from the main lobe, $r_0$ is the initial position of the main lobe, $\alpha$ is a decay parameter ensuring finite energy during propagation, and $\omega$ is the width of the main lobe. The effect of these intrinsic parameters on the generated CAB can be found in Figure S1 (Supporting Information). Subsequently, the CAB can be obtained by rotating Equation (1) around azimuthal angle $\Phi$ in the transverse plane. An approximate solution for the Fourier transform of the CAB can be derived using closed-form approximations:[21,41]

$$\psi(k) = \omega^2\left(\pm\frac{r_0}{\omega} + k^2\omega^2\right)\exp\left(-\alpha k^2\omega^2\right)$$

$$\sqrt{\frac{3kr_0 \pm k^3\omega^3}{3kr_0 \pm 3k^3\omega^3}}J_0\left(kr_0 \pm \frac{k^3\omega^3}{3}\right) \tag{2}$$

Equation (2) implies that a CAB transforms into a chirped Bessel beam in the far field. Considering a unique scenario, at the center of a 2D plane when the spatial frequency is $k \to 0$, Equation (2) only retains its dependent variable: $\Psi(k) \to J_0(kr_0)$. This finding that the light field exhibits oscillations that resemble those of a Bessel function. Hence, under self-focusing and self-diverging scenarios from a circular symmetric central region, the light field transforms from AFCA or ADCA into a BB, completing its transformation between different structures of nondiffraction beams. To encode the beam onto a metasurface, the phase profile is derived by obtaining the angle of the complex amplitude from Equation (1):

$$\varphi_{Airy} = \arg[\psi(r)] \tag{3}$$

### 2.2. Local and Global Phase Approach

For a conventional design approach, a metasurface must fill appropriate nanopillars at each site according to the phase function. Such phase profiles typically establish a global phase gradient across a specific dimension of light; for instance, the focusing phase deflects light in different directions across the sample plane, while the vortex phase undergoes azimuthal
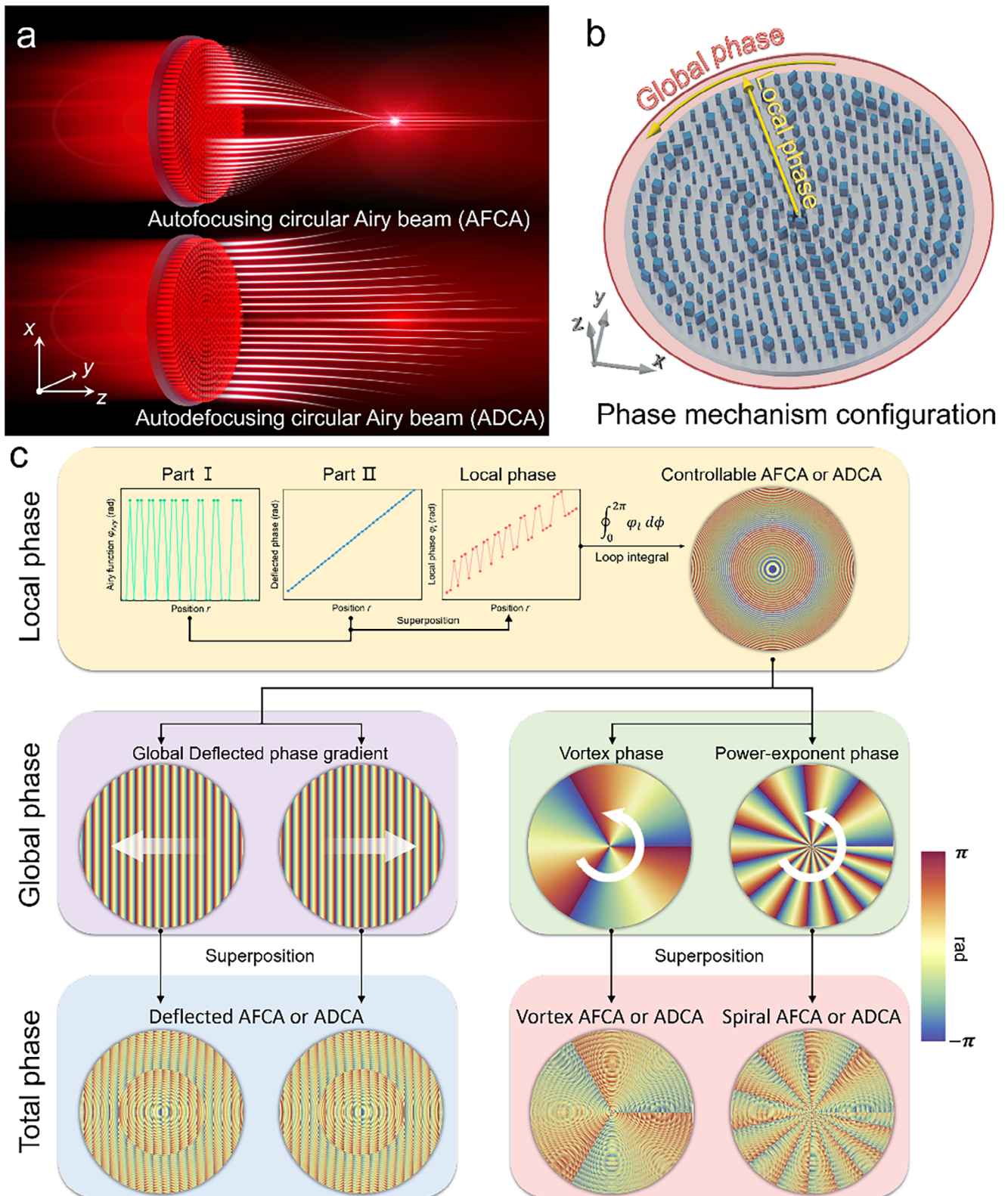
**Figure 1.** a) schematic illustration of AFCA (top) and ADCA (bottom). b) Phase configuration of the metasurface, where the yellow arrows represent the local phase, and the red areas denote the global phase. c) Flowchart for obtaining the total phase through combined modulation of the local and global phase.
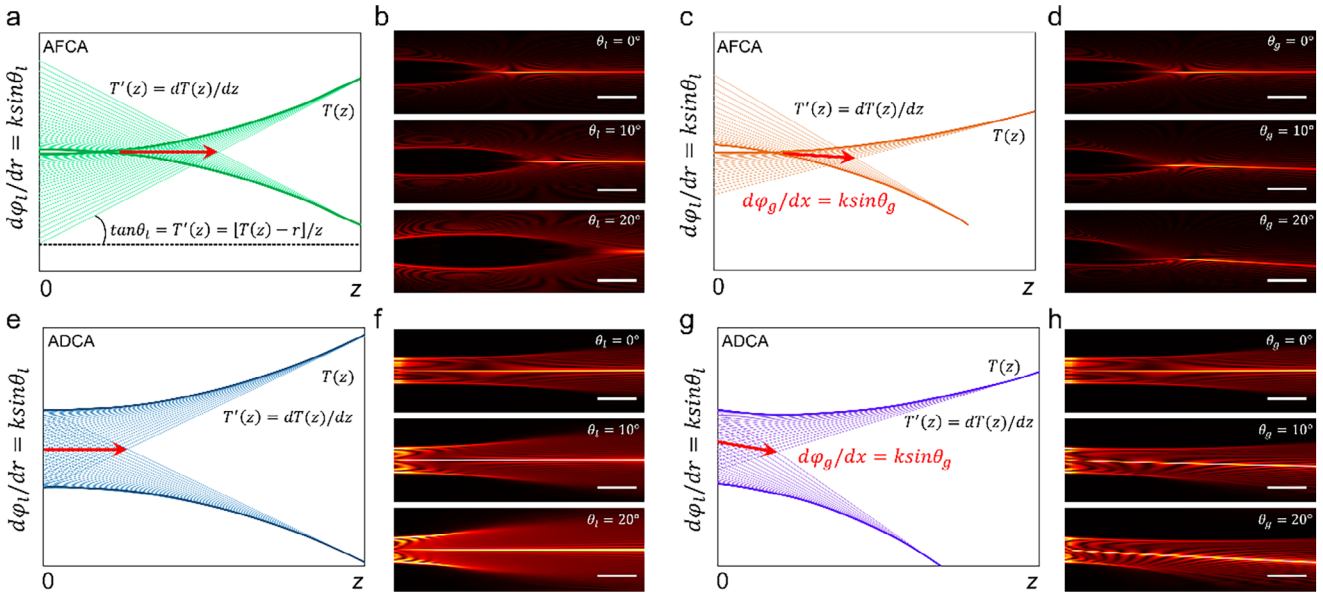
**Figure 2.** Illustrations of CABs modulated by local phase and global phase, respectively. (a,c,e,g) depicts schematic diagrams of the ray configurations, while (b,d,f,h) showcases the corresponding effect diagrams. Scale bar, 10 µm.

periodic variations within a 2D plane. Previous studies have shown that nondiffraction beams, such as 1D Airy or Bessel beams generated on the metasurface can be characterized in this manner and represented by a unified formula.[29,32,33] However, for CABs that exhibit both nondiffraction and self-bending properties and have self-focusing distances that can be manipulated, there is no analytical expression for their phase function. For this reason, we introduce a concept involving local and global phase considerations by accumulating the azimuthal phase of the 1D Airy beam to achieve the CAB, as depicted in Figure 1c. The local phase, in this context, represents a function of any amplitude and phase profile along the 1D direction and is determined by both the Airy function $\varphi_{Airy}$ and deflected phase $\varphi_d$:

$$\varphi_l(r) = \varphi_{Airy}(r) + \varphi_d(r) \tag{4}$$

with:

$$\varphi_d(r) = kr\sin\theta_l \tag{5}$$

where $r$ denotes the radial coordinates, and $\theta_l$ governs the deflection direction of the 1D Airy beam, thereby controlling the self-focusing position. To attain a CAB, it is necessary to perform a loop integration over $\varphi_l$ around the azimuthal infinary $d\phi$ based on Rayleigh–Sommerfeld integration:[45,46]

$$\psi_{CAB}(r,z) = \mathcal{F}^{-1}\left\{\mathcal{F}\left[\psi_i(r,z)\right]\right\} \times \mathcal{F}\left[h(R,z)\right] \tag{6}$$

Initial field $\psi_i(r,z)$ and impulse response $h(R,z)$ are functions of $R = (x, y, z)$, $R = |R|$ and propagating distance $z$:

$$\psi_i(r,z) = \oint_0^{2\pi} \varphi_l(r,z)\,d\phi \tag{7}$$

$$h(R,z) = \frac{z}{2\pi R}\frac{(1-ikR)}{R^2}\exp(ikR) \tag{8}$$

Based on this foundation, it is possible to further incorporate the global phase profile $\varphi_g$ to realize tilted, vortex, and spiral CABs. To exemplify the imposition of a global phase gradient, **Figure 2** illustrates the case of a CABs subjected to both local and global phase modulation. Assuming $T(z)$ is the trajectory of the Airy beam, the tangent at each point $T'(z) = dT(z)/dz$, is governed by $tan\theta_l$, thereby controlling the $\theta_l$ value of light ray deviation. From the ray tracing diagram shown in Figure 2a,c, it is evident that the central region of the CAB corresponds to the interference of the Airy beam, which is analogous to an axicon that reshapes and interferes with the wavefront of a plane wave to generate a Bessel beam. The direction of the red arrow represents the emission direction. Accordingly, we present light fields at a diameter of 100 µm when $\theta_l = 0°, 10°, 20°$, as shown in Figure 2b. However, applying a uniform phase gradient to all light rays alters the overall propagation direction of the CAB, which in turn changes the propagation direction of the subsequent Bessel component, as shown in Figure 2c,d. The total phase of the controllable propagation-deformable CAB can be written as follows:

$$\varphi_t(x,y,r) = \varphi_l(r) + \varphi_g(x,y) \tag{9}$$

where $\theta_g$ is the globally controlled deflection angle ($\theta_g = 0°, 10°, 20°$). The light rays deviate in a direction away from the optical axis. The phase of the spontaneously diverging CAB necessitates the assignment of opposite spatial coordinates in Equation (4). This assignment applies to both local and global phase modulation processes. As depicted in Figure 2e–h, both the trajectory of the AB and the BB are governed by the parameters $\theta_l$ and $\theta_g$. Similarly, in the 2D phase plane targeting both the x- and y-axes, it is possible to simultaneously manipulate the transverse structures of CABs and BBs by assigning vortex and

**ADVANCED
SCIENCE NEWS**

www.advancedsciencenews.com

LASER
& PHOTONICS
REVIEWS

www.lpr-journal.org

power-exponent phases to realize vortex or spiral AFCA and ADCA, with the following phase profile expression:[47–50]

$$\varphi_{vortex}(x, y) = l \cdot \arctan(y/x) \tag{10}$$

$$\varphi_{spiral}(x, y) = 4\pi m_2 \left[\arctan(y/x)/2\pi\right]^2 + m_1 m_2 \cdot \arctan(y/x) \tag{11}$$

where $x$ and $y$ are the coordinates of the nanopillars and $l$ is the topological charge of the vortex phase. The parameters $m_1$ and $m_2$ define the power-exponent phase, with the equivalent topological charge determined by $l = 2m_2 + m_1 m_2$. Through this procedure, we are not only able to generate axially symmetric AFCA or ADCA, realizing nondiffraction beams that evolve into BBs upon axial propagation, but can also reshape them in their transverse plane or along the propagation direction.

## 2.3. Tri-Functional CP-Multiplexing Case

To achieve the aforementioned phase modulation mechanisms, we integrate multitype CABs on a multifunctional spin-controlled single-layer metasurface, which also serves as circular polarization (CP) multiplexing surface. It is assumed that the spin angular momentum of light aligns with the orthogonal CP state of the wave in the classical representation. The designed sample is based on a thin amorphous silicon (a-Si) film deposited on fused quartz and arranged in a combination of propagation and geometric phases. The measured refractive index of a-Si is shown in Figure S2 (Supporting Information). Each sample features four channels for both crosspolarizations and copolarizations, allowing for independent control over three distinct phase profiles (unitarity). According to effective medium theory,[51] the nanopillars exhibit high levels of contrast in their refractive indices between orthogonal polarizations, and thus, their complex transmission properties are represented by the Jones matrix as follows:[52,53]

$$J(x, y) = R(\theta) \begin{bmatrix} T_o e^{i\varphi_o(x,y)} & 0 \\ 0 & T_e e^{i\varphi_e(x,y)} \end{bmatrix} R(-\theta) \tag{12}$$

where $(T_o, T_e)$ and $(\varphi_o, \varphi_e)$ represent the transmissive amplitude and phase shifts along the ordinary and extraordinary axes of nanopillars, respectively, and $R(\theta)$ is the rotation matrix. Next, we define phase difference $\delta = \varphi_o - \varphi_e$ and reference phase shift $\varphi_r = (\varphi_o + \varphi_e)/2$. By assuming $T_o = T_e = T$, the Jones matrix can be deduced as follows:

$$J(x, y) = Te^{i\varphi_r(x,y)} \begin{pmatrix} \cos\frac{\delta}{2} + i\cos 2\theta \sin\frac{\delta}{2} & -i\sin 2\theta \sin\frac{\delta}{2} \\ -i\sin 2\theta \sin\frac{\delta}{2} & \cos\frac{\delta}{2} - i\cos 2\theta \sin\frac{\delta}{2} \end{pmatrix} \tag{13}$$

For the CP incidence, the Jones matrix exerted by the CP bases $|L\rangle = [1 \ -i]^T/\sqrt{2}$ and $|R\rangle = [1 \ i]^T/\sqrt{2}$ can be simultaneously realized as cross-CP and co-CP channels, respectively; therefore, Equation (13) can be expressed as follows:

$$J(x, y) = Te^{i\varphi_r(x,y)} \cdot \begin{bmatrix} \cos\left(\frac{\delta}{2}\right) & i\sin\left(\frac{\delta}{2}\right) e^{-i2\theta} \\ i\sin\left(\frac{\delta}{2}\right) e^{i2\theta} & \cos\left(\frac{\delta}{2}\right) \end{bmatrix} \tag{14}$$

The phase difference $\delta$ governs both the polarization state of the incoming and outgoing beams and the carried phase profile. By judiciously selecting the appropriate phase difference and interlacing isotropic and anisotropic nanopillars to decouple CP polarization, a decoupled, independent phase profile with three distinct functionalities can be achieved. This approach facilitates the integration of structured AFCA and ADCA into the final phase configuration, then enabling precise generation and manipulation of the CP states. An in-depth derivation related to the Jones matrix can be found in Figure S3 (Supporting Information).

## 2.4. The Experimental Demonstration

According to the proposed CAB generation scheme, the experimental setup is shown in **Figure 3a**. The filtered continuous wave (CW) laser with a working wavelength of 1064 nm passes through a polarizer, is focused by an objective lens, and enters two prepared samples separately. After passing through an analyzer, the laser is recorded by a CCD camera. The insets in Figure 3a shows side and top views of nanopillars, which have consistent heights of 800 nm and periods of 600 nm. We encode the metasurface using suitable nanopillars by translating the total phase from Equation (9). The total phase profiles of AFCA and ADCA are depicted in Figure S4 (Supporting Information) and the selected nanopillar library parameters can be found in Figure S5 (Supporting Information). Figure 3b,c displays the optical and scanning electron microscopy (SEM) images of the fabricated samples, respectively.

The observed experimental results are presented in Figure 3d–f. Figure 3d,e,f sequentially depicts the simulation and experimental outcomes for conventional AFCA, vortex AFCA, and spiral AFCA, respectively. Here, the two polarization channels exhibit the same channel phenomena, while the cross-polarized channels display independent field distributions. We select the transverse planes at intervals of 10 µm from $z = 5$ µm to $z = 45$ µm to observe their self-focusing evolution to BB phenomena. The results indicate that the Airy rings have pronounced intensity fluctuations in the near field, manifesting as nested multiple rings. However, these rings do not alter the global-phase-modulated light field. The rings exhibit normal focus, vortex, and spiral shapes near the optical axis. As the propagation distance increases, the energies of the outer rings gradually concentrate inward until they contract into a single bright ring with a global phase. From this position onward, the self-focusing effect of AFCA causes the light spot to evolve into a BB-like profile, which persists for a certain distance without diffraction, attesting to its BB-like characteristics. To characterize the topological charge of the generated vortex BB in Figure 3e, we implement a spherical wave interferometric setup, as depicted in Figures S5a,b and S6 (Supporting Information). It is worth noting that for spiral AFCA, owing to the inherent chirality of the spiral light fields generated by power exponential terms, when superimposed onto the CAB through the global phase, it exhibits asymmetry in the longitudinal light fields. Thus, we present both the x-z and y-z planes in Figure 3f. To provide a detailed representation of the evolution process, Figure 3g,h displays the simulated and experimental full width at half maximum (FWHM) results, indicating a close alignment between the
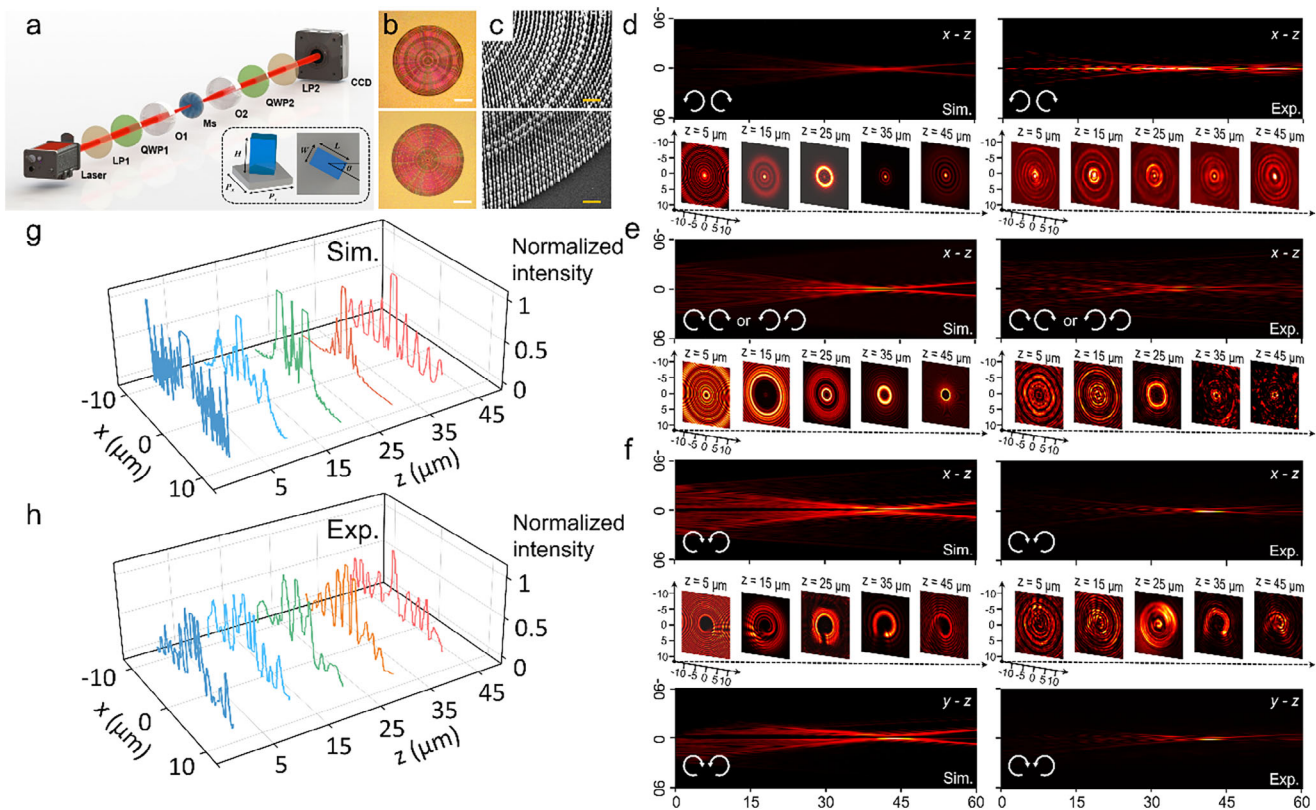
**Figure 3.** Experimental characterization of sample and nanophotonic fields. a) optical setup for observing CABs in different polarization channels. LP represents linear polarizer, QWP denotes quarter-wave plate, and O refers to the objective with NA = 0.4. b,c) top view and bottom views respectively present the optical microscopy (scale bar, 20 μm) and SEM (scale bar, 5 μm) characterizations of AFCA and ADCA samples. d,e,f) simulated and experimental results of tri-functional metasurface for generating AFCA, vortex AFCA, and spiral AFCA. While the co-CP yields the same results due to the equality of the diagonal elements in the Jones matrix. g,h) simulated and experimental measurement of FWHM results for AFCA at different transverse planes.

measured results and the anticipated light field. Finally, a typical profile of a BB is shown.

Turning to **Figure 4**, the near field of ADCA consists of an outer bright Airy ring, with its intensity gradually decreasing inward, while its center is dominated by the globally phase-induced light field. As propagation continues, the outer Airy ring progressively expands, with decreasing intensity. Near the optical axis, the BB-like profile formed due to sidelobe interference maintains its diffraction-free nature, preserving its spot size and propagating farther than the BB generated by AFCA. Overall, ADCA starts with the outermost Airy ring, which exhibits the highest level of intensity, leading to the obliteration of the Airy rings after diverging and eventually evolving into BB. Similarly, we detect the topological charge for the case in Figure 4b, and the experimental results are shown in Figure S5c and S6 (Supporting Information). For spiral ADCA, Figure 4c depicts the propagation fields in two longitudinal planes. Figure 4d,e presents the simulated and experimentally measured FWHM results, with any experimental discrepancies attributed to measurement errors, which do not affect the ADCA evolution phenomena. A comparative analysis of the BB-like beams, generated upon the completion of the AFCA and ADCA evolutionary processes and compared with the ideal BB, is also provided. Detailed information on this comparison is available in Figure S7 (Supporting Information).

## 2.5. The Self-Healing of Sample Defects

The self-healing of defects is a hallmark feature of nondiffraction light beams, ensuring that obstructions in the propagation direction do not influence their far-field intensity distributions. This phenomenon is particularly significant in the domain of nanophotonics, where device performance is often compromised by fabrication defects and inaccuracies, thereby affecting experimental outcomes. Therefore, we demonstrate that the self-healing attributes of CAB propagated along the optical axis are not limited by the precision of fabrication, allowing a certain degree of fabrication error and exhibiting robustness during propagation.

For proof-of-concept, we design three kinds of AFCA samples with ring, line, and area defects to characterize their optical properties, as shown in **Figure 5**. The ring defect in Figure 5a can be viewed as a missing local phase at a particular coordinate with a circumferential global phase defect. This defect mimics the robustness of 1D Airy beams against defects without affecting the azimuthally global periodicity; that is, the rest of the global phase still fulfill the periodic azimuthal phase gradient, sufficiently generating OAM. Although the near-field displays the imperfections of the spots, as shown in the first column of Figure 5b, owing to the autofocusing effect, these imperfections vanish as

ADVANCED
SCIENCE NEWS

www.advancedsciencenews.com

LASER
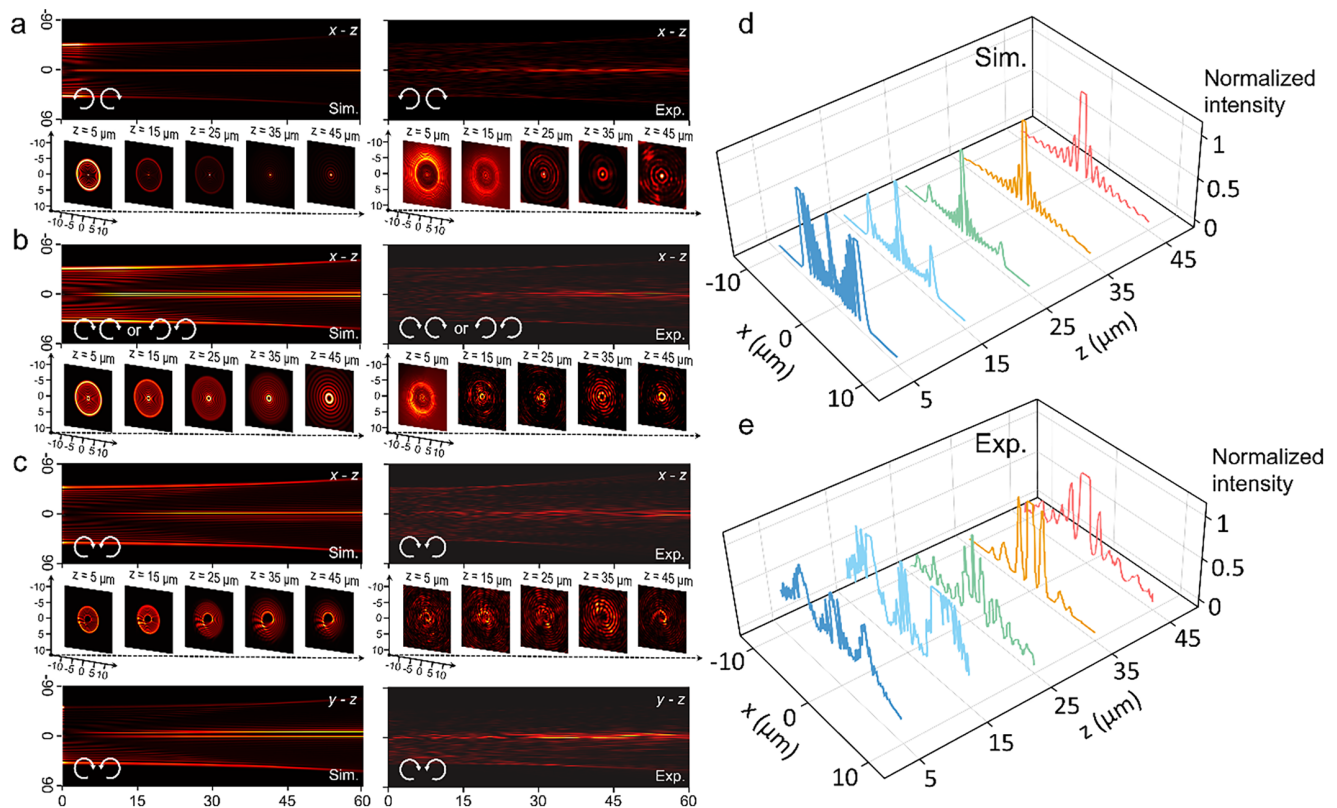& PHOTONICS
REVIEWS

www.lpr-journal.org

**Figure 4.** Experimental characterization of ADCA. a–c) From top to bottom: longitudinal and transverse patterns of ADCA, vortex ADCA, and spiral ADCA, respectively. d,e) Simulated and experimental results of the FWHM for ADCA at different propagation planes.

the light passes into the far-field, converging into the predicted patterns.

The line defect illustrated in Figure 5c signifies that the local phase has not fully integrated into the $0-2\pi$ interval during its annular integration. Nonetheless, due to the circular symmetry of CABs, the interference zones of Airy rings remain, ensuring BB generation at $z = 45$ μm, leading to the ultimate recovery of the light field. For channels two and three, the line defect is analogous to a periodic angular phase gradient centered around the origin lacking a radial phase value, which has no impact on the overall phase modulation. The area defect shown in Figure 5e signifies multiple local phase defects in the corresponding 1D ABs. However, these defects affect the global phase, resulting in some azimuthal phase value deficits, as shown in Figure 5f. The spot is incomplete from $z = 5$ μm to $z = 35$ μm, but due to a small area of purposefully generated defects, the formation processes of many BBs are ultimately unaffected.

Importantly, our findings regarding defect robustness pertain only to small-scale, unpredictable errors that occur during the nanofabrication processes and do not imply tolerance to the absence of large portions of nanopillars, which parallels photonic topological insulators, in that the resulting light field can be maintained. Given their nondiffraction characteristics, these results offer significant insights into laser direct writing in nanolithography, providing a layer of reliability and robustness in device fabrication.

## 3. Conclusion

To conclude, we propose a state-of-the-art metasurface design strategy that ingeniously combines both local and global phase modulations to yield propagation-deformable circular Airy beams. The theoretical and experimental results vividly demonstrate the conversion of autofocusing and autodefocusing Airy beams into Bessel beams during propagation along the optical axis. In addition, we successfully utilize angular momentum to reshape CABs by controlling the global phase, revealing the potential for 3D structural manipulation of optical fields. Furthermore, the CABs are robust to various defects, highlighting their potential in applications such as laser direct writing etching to create intricate waveguides and gratings in microfabrication and nanofabrication processes. Our work stands as a pivotal stride in reshaping the utilization of nondiffraction light and amplifying the multifunctionalities of metasurfaces. We lay a robust foundation for the development of advanced on-chip nano-optical platforms and for the expansion of innovative fabrication techniques.

## 4. Experimental Section

*Numerical Simulation*: This metasurface sample was fabricated by positioning a-Si nanopillars on a fused-silica substrate. The modulation phase generated was associated with the structural dimensions of the nanopillar. To discern the optimal parameters conducive to the intended
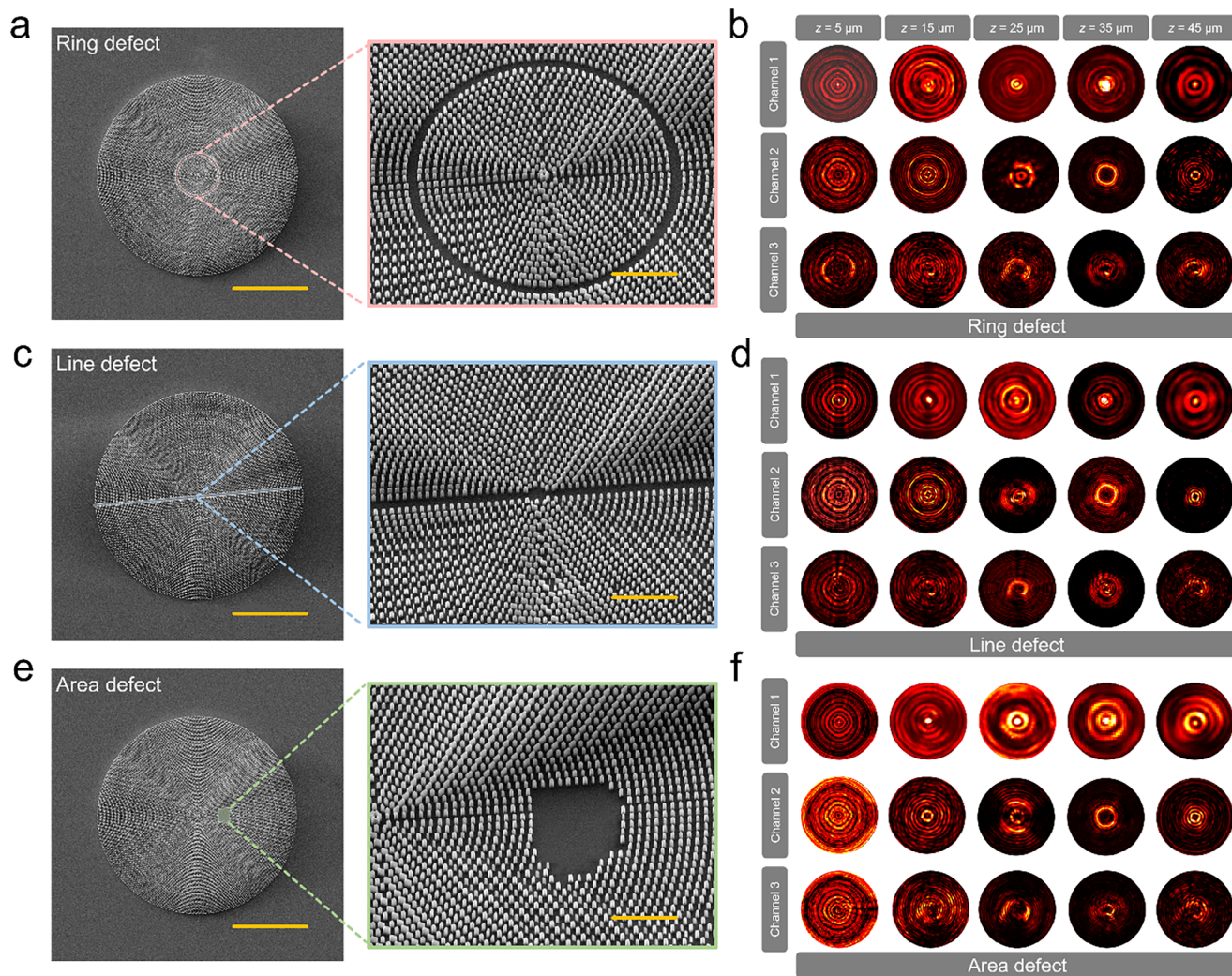
**ADVANCED
SCIENCE NEWS**

www.advancedsciencenews.com

www.lpr-journal.org

LASER
& PHOTONICS
REVIEWS

**Figure 5.** Sample characterization and experimental measurement of defective metasurfaces, displayed from top to bottom: ring, linear, and area defects. a,c,e) the SEM and their partial magnifications for the three types of defects, respectively, left scale bar, 20 μm, right scale bar, 5 μm. b,d,f) transverse distributions in different cross-sections along the optical path within the three channels.

phase modulation, arrays of nanopillars with distinct geometric configurations were modeled using the Finite–Difference Time-Domain (FDTD) method. These nanopillars were organized in a square lattice having a lattice constant of 600 nm and a uniform height of 800 nm. The refractive indices of a-Si utilized were within the near-infrared wavelength range, determined from ellipsometry assessments of an a-Si thin film. The boundary conditions were designated as periodic in the in-plane directions to model the periodic nanopillar arrays, while for transmission situations, the boundary conditions were identified as perfect match layers in the light incidence direction. A plane wave with a wavelength of 1064 nm was employed to discern the transmission coefficients and phase shifts along the x- and y-axes, corresponding to the lateral and vertical dimensions of nanopillars, as depicted in Figure S2 (Supporting Information).

*Metasurface Fabrication*: The silica-based wafer underwent ultrasonic cleansing using acetone, alcohol, and deionized water. This was succeeded by the application of an 800 nm layer of amorphous silicon ($\alpha$-Si) onto the pristine silica wafer via Plasma-Enhanced Chemical Vapor Deposition (Oxford PlasmaPro 100 PECVD). Afterward, the silicon surface received a spin-coated layer of conductive, positive electron-beam resist (ZEP520A, Zeon) ≈200 nm thick. The intended metasurface designs were then etched

onto the CSAR-6200 resist using an Electron Beam Lithography (EBL) system, specifically the Elionix ELS-F125-G8. Post-exposure, the patterns were developed by a photoresist developer, transferring them onto a chromium (Cr) mask. Subsequent steps involved depositing a patterned chromium (Cr) layer onto the sample via Electron Beam Evaporation (EBE), creating a Cr mask on the thin film for further etching processes. The etching was performed using an Inductively Coupled Plasma Reactive Ion Etcher (ICP-RIE) with a mixture of O2 and CHF3 gases. Finally, the remaining Cr mask was removed using a cerium ammonium nitrate solution, completing the fabrication of this metasurface.

*Experimental Setup*: To initiate the experimental procedures, a supercontinuum laser (Energetiq, EQ-99XFC) was utilized, which, post traversing through an near-infrared filter (Thorlabs, FLH1064-3), furnished a near-infrared laser at 1064 nm. The methodology involved the strategic positioning of a Linear Polarizer (LP1, Thorlabs LPIREA100-C) and a Quarter-wave Plate (QWP1, Thorlabs WPQSM05-1064) prior to the sample to modulate the input polarization meticulously. Subsequently, an objective lens (O1, Mitutoyo MY5X-822) was deployed to converge the beam dimensions coherently to the size of the sample. Considering the sub-millimeter dimensions of the reconstructed images, a microscope

objective (O2, Mitutoyo MY5X-824) with a numerical aperture (NA) of 0.4 was situated posterior to the sample to capture the complex amplitude distribution of the output light via a CCD (HAMAMATSU PHOTONICS C12741-03). The precise manipulation of the polarization states of input and output light was achieved by the rotation of QWP2 and LP2, thereby facilitating the selection of three distinct polarization functionalities.

## Supporting Information

Supporting Information is available from the Wiley Online Library or from the author.

## Acknowledgements

## Conflict of Interest

The authors declare no conflict of interest.

## Data Availability Statement

The data that support the findings of this study are available from the corresponding author upon reasonable request.

## Keywords

3D light-field manipulation, deformable non-diffractive beam, local and global phase modulation, robustness of defect, tri-functional metasurface

[1] A. Forbes, M. de Oliveira, M. R. Dennis, *Nat. Photonics* **2021**, *15*, 253.
[2] M. Mazilu, D. J. Stevenson, F. Gunn-Moore, K. Dholakia, *Laser Photonics Rev.* **2010**, *4*, 529.
[3] J. Durnin, *J. Opt. Soc. Am.* **1987**, *4*, 651.
[4] R. M. Power, J. Huisken, *Nat. Methods* **2017**, *14*, 360.
[5] H. Jia, X. Yu, Y. Yang, X. Zhou, S. Yan, C. Liu, M. Lei, B. Yao, *J Biophotonics* **2019**, *12*, e201800094.
[6] R. Cao, J. Zhao, L. Li, L. Du, Y. Zhang, Y. Luo, L. Jiang, S. Davis, Q. Zhou, A. de la Zerda, L. V. Wang, *Nat. Photonics* **2022**, *17*, 89.
[7] M. Pahlevaninezhad, Y. W. Huang, M. Pahlevani, B. Bouma, M. J. Suter, F. Capasso, H. Pahlevaninezhad, *Nat. Photonics* **2022**, *16*, 203.
[8] O. Brzobohatý, V. Karásek, M. Šiler, L. Chvátal, T. Čižmár, P. Zemánek, *Nat. Photonics* **2013**, *7*, 123.
[9] S. Xia, A. Ramachandran, S. Xia, D. Li, X. Liu, L. Tang, Y. Hu, D. Song, J. Xu, D. Leykam, S. Flach, Z. Chen, *Phys. Rev. Lett.* **2018**, *121*, 263902.
[10] F. Xin, F. Flammini, F. Di Mei, L. Falsi, D. Pierangeli, A. J. Agranat, E. DelRe, *Phys. Rev. Appl.* **2019**, *11*, 024011.
[11] M. Duocastella, C. B. Arnold, *Laser Photonics Rev.* **2012**, *6*, 607.
[12] G. A. Siviloglou, J. Broky, A. Dogariu, D. N. Christodoulides, *Phys. Rev. Lett.* **2007**, *99*, 213901.
[13] G. A. Siviloglou, D. N. Christodoulides, *Opt. Lett.* **2007**, *32*, 979.
[14] N. K. Efremidis, Z. Chen, M. Segev, D. N. Christodoulides, *Optica* **2019**, *6*, 686.
[15] S. Jia, J. C. Vaughan, X. Zhuang, *Nat. Photonics* **2014**, *8*, 302.
[16] T. Vettenburg, H. I. Dalgarno, J. Nylk, C. Coll-Llado, D. E. Ferrier, T. Cizmar, F. J. Gunn-Moore, K. Dholakia, *Nat. Methods* **2014**, *11*, 541.
[17] J. Wang, X. Hua, C. Guo, W. Liu, S. Jia, *Optica* **2020**, *7*, 790.
[18] R. Ivaskeviciute-Povilauskiene, P. Kizevicius, E. Nacius, D. Jokubauskis, K. Ikamas, A. Lisauskas, N. Alexeeva, I. Matulaitiene, V. Jukna, S. Orlov, L. Minkevicius, G. Valusis, *Light: Sci. Appl.* **2022**, *11*, 326.
[19] J. Baumgartl, M. Mazilu, K. Dholakia, *Nat. Photonics* **2008**, *2*, 675.
[20] Y. Liang, S. Yan, Z. Wang, R. Li, Y. Cai, M. He, B. Yao, M. Lei, *Rep Prog Phys* **2020**, *83*, 032401.
[21] P. Zhang, J. Prakash, N. K. Efremidis, D. N. Christodoulides, Z. Chen, *Opt. Lett.* **2011**, *36*, 2883.
[22] J. C. Gutiérrez-Vega, M. D. Iturbe-Castillo, G. A. Ramírez, E. Tepichín, R. M. Rodríguez-Dagnino, S. Chávez-Cerda, G. H. C. New, *Opt. Commun.* **2001**, *195*, 35.
[23] C. Alpmann, R. Bowman, M. Woerdemann, M. Padgett, C. Denz, *Opt. Express* **2010**, *18*, 26084.
[24] A. Bencheikh, S. Chabou, O. C. Boumeddine, H. Bekkis, A. Benstiti, L. Beddiaf, W. Moussaoui, *J Opt Soc Am A* **2020**, *37*, C7.
[25] L. Li, T. Li, S. M. Wang, C. Zhang, S. N. Zhu, *Phys. Rev. Lett.* **2011**, *107*, 126804.
[26] A. Minovich, A. E. Klein, N. Janunts, T. Pertsch, D. N. Neshev, Y. S. Kivshar, *Phys. Rev. Lett.* **2011**, *107*, 116802.
[27] N. Yu, P. Genevet, M. A. Kats, F. Aieta, J.-P. Tetienne, F. Capasso, Z. Gaburro, *Science* **2011**, *334*, 333.
[28] S. Sun, Q. He, S. Xiao, Q. Xu, X. Li, L. Zhou, *Nat. Mater.* **2012**, *11*, 426.
[29] W. T. Chen, M. Khorasaninejad, A. Y. Zhu, J. Oh, R. C. Devlin, A. Zaidi, F. Capasso, *Light: Sci. Appl.* **2017**, *6*, e16259.
[30] S. Wang, P. C. Wu, V. C. Su, Y. C. Lai, C. Hung Chu, J. W. Chen, S. H. Lu, J. Chen, B. Xu, C. H. Kuan, T. Li, S. Zhu, D. P. Tsai, *Nat. Commun.* **2017**, *8*, 187.
[31] S. Wang, P. C. Wu, V. C. Su, Y. C. Lai, M. K. Chen, H. Y. Kuo, B. H. Chen, Y. H. Chen, T. T. Huang, J. H. Wang, R. M. Lin, C. H. Kuan, T. Li, Z. Wang, S. Zhu, D. P. Tsai, *Nat. Nanotechnol.* **2018**, *13*, 227.
[32] T. Li, X. Li, S. Yan, X. Xu, S. Wang, B. Yao, Z. Wang, S. Zhu, *Phys. Rev. Appl.* **2021**, *15*, 014059.
[33] Q. Fan, W. Zhu, Y. Liang, P. Huo, C. Zhang, A. Agrawal, K. Huang, X. Luo, Y. Lu, C. Qiu, H. J. Lezec, T. Xu, *Nano Lett.* **2019**, *19*, 1158.
[34] J. Wen, L. Chen, B. Yu, J. B. Nieder, S. Zhuang, D. Zhang, D. Lei, *ACS Nano* **2021**, *15*, 1030.
[35] T. Li, J. J. Kingsley-Smith, Y. Hu, X. Xu, S. Yan, S. Wang, B. Yao, Z. Wang, S. Zhu, *Opt. Lett.* **2023**, *48*, 255.
[36] T. Badloe, J. Seong, J. Rho, *Nano Lett.* **2023**, *23*, 6958.
[37] A. H. Dorrah, N. A. Rubin, A. Tamagnone, A. Zaidi, F. Capasso, *Nat. Commun.* **2021**, *12*, 6249.
[38] J. Yang, R. Zhao, Y. Li, H. Xiong, Y. Li, X. Li, J. Li, Y. Wang, L. Huang, *Adv. Opt. Mater.* **2023**, *11*, 2202896.
[39] C.-Y. Hwang, K.-Y. Kim, B. Lee, *Opt. Express* **2011**, *19*, 7356.

[40] I. Chremmos, P. Zhang, J. Prakash, N. K. Efremidis, D. N. Christodoulides, Z. Chen, *Opt. Lett.* **2011**, *38*, 3675.

[41] Y. Jiang, X. Zhu, W. Yu, H. Shao, W. Zheng, X. Lu, *Opt. Express* **2015**, *23*, 29834.

[42] A. Chong, W. H. Renninger, D. N. Christodoulides, F. W. Wise, *Nat. Photonics* **2010**, *4*, 103.

[43] J. Pan, H. Wang, Y. Shen, X. Fu, Q. Liu, *Appl. Phys. Lett.* **2022**, *121*, 141102.

[44] P. Zhang, Q. Guo, H. Wu, Z. Gong, B. Nie, Y. Hu, Z. Chen, J. Xu, *Phys. Rev. Lett.* **2023**, *131*, 087201.

[45] M. Born, E. Wolf, *Principles of Optics*, Cambridge University Press, Cambridge, United Kingdom **1999**.

[46] N. Chen, C. Wang, W. Heidrich, *Opt. Express* **2022**, *30*, 37727.

[47] P. Li, S. Liu, T. Peng, G. Xie, X. Gan, J. Zhao, *Opt. Express* **2014**, *22*, 7598.

[48] G. Lao, Z. Zhang, D. Zhao, *Opt. Express* **2016**, *24*, 18082.

[49] H. Wang, L. Tang, J. Ma, H. Hao, X. Zheng, D. Song, Y. Hu, Y. Li, Z. Chen, *APL Photonics* **2020**, *5*, 016102.

[50] X. Fang, H. Ren, K. Li, H. Luan, Y. Hua, Q. Zhang, X. Chen, M. Gu, *Adv. Opt. Photonics* **2021**, *13*, 772.

[51] M. Khorasaninejad, F. Capasso, *Science* **2017**, *358*, eaam8100.

[52] J. P. Balthasar Mueller, N. A. Rubin, R. C. Devlin, B. Groever, F. Capasso, *Phys. Rev. Lett.* **2017**, *118*, 113901.

[53] T. Li, X. Xu, B. Fu, S. Wang, B. Li, Z. Wang, S. Zhu, *Photonics Research* **2021**, *9*, 1062.